

# Deuterium addition to liquid Li-Sn alloys: Implications for plasma-facing applications

Beatriz G. del Rio,<sup>1</sup> Gopalakrishnan Sai Gautam,<sup>1</sup> and Emily A. Carter<sup>2\*</sup>

<sup>1</sup>Department of Mechanical and Aerospace Engineering, Princeton University, Princeton, New Jersey 08544-5263, USA

<sup>2</sup>School of Engineering and Applied Science, Princeton University, Princeton, New Jersey 08544-5263, USA

\*Corresponding author: [eac@princeton.edu](mailto:eac@princeton.edu)

## Abstract

Liquid metals are being explored actively as candidates for plasma-facing components (PFCs) in fusion reactors. Recently, Li-Sn alloys have appeared as promising alternatives that could overcome some of the challenges faced by the well-studied liquid Li system, namely, a vapor pressure that limits the operating temperature and a high hydrogen isotope retention. However, only scarce data (experimental or theoretical) are available concerning the performance of Li-Sn alloys, specifically only for the compositions of  $\text{Li}_{30}\text{Sn}_{70}$  and  $\text{Li}_{20}\text{Sn}_{80}$ , related to their bonding and retention of deuterium (D). Here, we present a comprehensive, first-principles molecular-dynamics study of static and dynamic properties of liquid  $\text{Li}_{30}\text{Sn}_{70}$  at various D concentrations. We observe the formation of  $\text{D}_2$  gas bubbles for  $\beta$  in  $\text{Li}_{30}\text{Sn}_{70}\text{D}_\beta$  greater than 22.5 along with Li segregation towards  $\text{D}_2$  bubbles. To understand the effect of Sn addition on D retention in Li-Sn alloys, we perform a thermodynamic evaluation of maximum D retention in Li-rich Li-Sn alloys. Overall, this work will provide useful data and guidance in the development of Li-Sn PFCs in fusion reactors.

## 1. Introduction

Fusion energy could be a key technology later this century for overcoming the environmental and energy crisis faced by humanity [1]. For decades, scientific research has focused on stabilizing the plasma at a temperature of thousands of degrees inside a fusion reactor, where a significant challenge is the type of material used for the interior wall of such reactors. Two main pathways have been explored so far: 1) the use of materials with high melting points, such as tungsten; and 2) the use of liquid metals with low melting points, such as lithium (Li). The usage of high-melting-point materials, while more common, presents various limitations such as brittleness and erosion [2] due to interactions with the plasma and subsequent neutron fluxes. These limitations may be overcome by employing liquid metals, which provide self-replenishing and self-healing plasma-facing surfaces [3] with no susceptibility to neutron damage.

Several tokamak facilities are investigating the use of liquid metals as plasma facing components (PFCs) [4–6], where an important metric in determining the metal of choice is the atomic number (Z). Low-Z metals can cause fuel dilution of the fusion plasma, while high-Z elements can result in plasma contamination and eventual radiative collapse [7,8]. The state of the art, so far, is liquid lithium due to its promising characteristics, such as a low melting point and a relatively low vapor pressure [3,9–11], and exhibiting a low-Z. Another candidate besides liquid Li is liquid tin (Sn), a high-Z metal that exhibits vapor pressure lower than liquid Li [3], allowing a higher operating temperature, and retains lower amounts of deuterium (D) compared to Li [12]. Other possible candidates considered include liquid gallium (Ga), liquid  $\text{Li}_{17}\text{Pb}_{83}$  alloy, and the molten salts Flibe and Flinabe [3,13]. The use of Flibe and Flinabe was motivated by the need to reduce the chemical activity of Li with water while maintaining a low melting point. However, the viscosity of Flibe rapidly increases with the addition of  $\text{BeF}_2$  [14], inhibiting the replenishing and healing properties of the molten salt.  $\text{Li}_{17}\text{Pb}_{83}$ , while more stable chemically than pure Li, has a thermal conductivity considerably lower than liquid Li [15]. Additionally, it is desirable for any liquid metal system to contain Li in order to provide adequate tritium for the fusion reactor [16], ruling out the use of pure Sn or Ga.

Recently, the liquid Li-Sn alloy has attracted attention due to its improved properties over liquid Li and liquid Sn: a lower vapor pressure than Li [6,17,18], a reduction of plasma contamination from high-Z Sn atoms due to Li segregation to the alloy surface [19,20], and a significantly lower D retention than pure Li [12]. Since many properties of liquid Li-Sn alloys are still unknown, we previously studied various properties of liquid Li-Sn *via* first-principles molecular dynamics (FPMD) simulations at the two concentrations of interest for PFC applications,  $\text{Li}_{30}\text{Sn}_{70}$  and  $\text{Li}_{20}\text{Sn}_{80}$  [21], and obtained good agreement with available experimental data. Nevertheless, it still is essential to know the effect of D addition on the Li-Sn alloy properties, especially D bonding and retention, in order to determine the suitability of Li-Sn alloys as PFCs.

Previous experimental work has shown a low retention of the different hydrogen (H) isotopes in liquid Li-Sn alloys. For example, Tabarés and coworkers measured the H retention in liquid  $\text{Li}_{20}\text{Sn}_{80}$  to be  $\sim 0.01\%$   $\text{H}/(\text{Sn}+\text{Li})$  for temperatures lower than 723 K [22], similar to Loureiro *et al.*'s D retention measurements in liquid  $\text{Li}_{30}\text{Sn}_{70}$  at 658 K where only  $\sim 1.73 \times 10^{-4}$  of the incident D was retained [12]. Kang and Terai [23,24] reported a tritium diffusivity of  $\sim 1.27 \times 10^{-9} \text{ m}^2/\text{s}$  in liquid  $\text{Li}_{20}\text{Sn}_{80}$  at 973 K by using an in-reactor tritium release experiment, while diffusivity of H or D and shear viscosity of the liquid alloy system are not yet available in the literature.

In the current work, we performed a detailed FPMD study of liquid  $\text{Li}_{30}\text{Sn}_{70}$  at four different D concentrations and temperatures, based on forces derived from Kohn-Sham density functional theory

(KSDFT), to understand the effect of D addition to liquid  $\text{Li}_{30}\text{Sn}_{70}$ . Specifically, we observe  $\text{D}_2$  gas formation for  $\beta$  (in  $\text{Li}_{30}\text{Sn}_{70}\text{D}_\beta$ ) greater than 22.5 within the liquid alloy, along with Li segregation towards the  $\text{D}_2$  molecules. We also performed a thermodynamic evaluation of maximum D retention in Li-rich Li-Sn alloys to understand the effect of Sn on D retention. Recently, KSDFT-based FPMD simulations by Chen *et al.* were used to calculate structural and dynamic properties when D is added to liquid Li [25]; the authors predicted a high D retention in liquid Li, up to a 1:1 D:Li ratio. The theoretical predictions [25] offered support to experimental observations of a reduced Li sputtering yield [26,27], which may be caused by the formation of LiD precipitates under high D fluxes impinging on liquid Li films. Similarly, we hope that our predictions here will provide useful data, support, and guidance in the development of Li-Sn PFCs.

The paper is organized as follows. We introduce the computational method, simulation details, and theory framework used in evaluating each liquid property in section 2. All simulation results along with the discussion are presented in section 3, where we will address three main questions: 1) How does the presence of Sn atoms affect the affinity of Li for D? 2) How are the diffusivities of each species affected by the concentration of D? and 3) How is the viscosity affected by the presence and retention of D? We end in section 4 by drawing conclusions, including implications the results have for using liquid Li-Sn alloys as PFCs.

## 2. Methodology

### 2.1 Computational method

All of the molecular dynamics (MD) simulations are performed within the Born-Oppenheimer approximation, where the total energy is computed as the sum of the classical kinetic energy of the ions (the positively charged, screened nuclei), the Coulomb repulsion energy between the ions, and the ground-state energy of the electrons in the presence of the ions. The electronic ground-state energy can be evaluated accurately within KSDFT [28], where the total electronic energy is expressed as a functional of the electron density,  $n(\vec{r})$ , with four different contributions:

$$E[n(\vec{r})] = T_s[n(\vec{r})] + E_H[n(\vec{r})] + E_{\text{ext}}[n(\vec{r})] + E_{\text{XC}}[n(\vec{r})] \quad (1)$$

Here,  $T_s$  is the kinetic energy of a non-interacting electronic system,  $E_H$  is the Hartree term due to the electrostatic repulsion between the electrons,  $E_{\text{ext}}$  is the electron-ion interaction energy due to the potential created by the ions, and  $E_{\text{XC}}$  is the electron exchange-correlation (XC) energy. KSDFT is an orbital-based theory, which accounts for its accuracy but makes the method scale cubically with the number of electrons, thus imposing severe limitations on the system size to typically no more than a few hundred atoms.

We used the Vienna *ab initio* simulation package (VASP) [29,30] to perform all of our calculations, where  $E_{\text{ext}}$  is modelled using the projector-augmented-wave (PAW) method [31,32]. We employed the

default PAW potentials for Li and Sn, while the D nucleus is modelled by the H PAW potential using the mass of the D isotope. For the XC functional, we used the generalized gradient approximation with a parametrization derived from the Perdew-Burke-Ernzerhof (PBE) [33] XC revised for solids, PBEsol [34], which performs better than PBE or the local density approximation [35,36] for the Li-Sn alloy [21]. All calculations use periodic boundary conditions, with the  $k$ -point meshes in the Brillouin zone generated with the Monkhorst-Pack scheme [37], where the generated meshes converged the total energies to less than 1 meV/atom. The kinetic energy cutoff for the plane wave basis was 400 eV. We used the Fermi surface smearing method of Methfessel-Paxton [38], with a smearing width of 0.2 eV.

To validate our theoretical framework, we evaluated the formation enthalpies of various binary, solid Li-Sn alloys and solid LiH at 0 K and compared them to experimental thermodynamic data at 298 K (Table 1). The binary compounds studied and the number of atoms within the respective unit cells (space groups given in parentheses) were: rock salt LiH, a unit cell with two atoms;  $\text{Li}_7\text{Sn}_2$  (Cmmm), 18 atoms;  $\text{Li}_{13}\text{Sn}_5$  (P-3m1), 18 atoms;  $\text{Li}_5\text{Sn}_2$  (R-3m), seven atoms;  $\text{Li}_7\text{Sn}_3$  (P2<sub>1</sub>/m), 20 atoms; LiSn (I4<sub>1</sub>/amd), six atoms; and  $\text{Li}_2\text{Sn}_5$  (P4/mbm), 14 atoms. For relaxing all the structures we used a  $k$ -point density of  $70/\text{\AA}^{-3}$  in each lattice vector direction. All solid alloy structures were obtained from the Inorganic Crystal Structure Database [39].

Table 1. Enthalpies of formation in eV per formula unit of LiH and solid intermetallic Li-Sn alloys. Experimental data for Li-Sn intermetallic compounds from Yin *et al.* [40]. Note that the experimental formation enthalpy of solid LiH is similar to that of solid LiD [41].

$\Delta H_f$ (eV/f. u.)	LiH	$\text{Li}_7\text{Sn}_2$	$\text{Li}_{13}\text{Sn}_5$	$\text{Li}_5\text{Sn}_2$	$\text{Li}_7\text{Sn}_3$	LiSn	$\text{Li}_2\text{Sn}_5$
<b>KSDFT</b>	-0.897	-3.462	-7.497	-2.892	-4.098	-0.706	-1.508
<b>Exp.</b>	-0.981	-3.892	-7.443	-2.877	-4.082	-0.744	-1.584

The theoretically predicted enthalpies of formation in Table 1 compare satisfactorily with available experimental data, especially for the cases of LiH,  $\text{Li}_{13}\text{Sn}_5$ ,  $\text{Li}_5\text{Sn}_2$ ,  $\text{Li}_7\text{Sn}_3$ , LiSn, and  $\text{Li}_2\text{Sn}_5$ , where the discrepancies are of a few tens of meV/f.u. For the case of  $\text{Li}_7\text{Sn}_2$ , the discrepancy is larger. These discrepancies are partly due to our neglect of the temperature dependence of the enthalpy (0 K versus 298 K) and pressure-volume contributions. In light of the overall good agreement obtained for the enthalpy of formation, especially for solid- $\text{Li}_2\text{Sn}_5$  (which has the nearest composition to our composition of interest,  $\text{Li}_{30}\text{Sn}_{70}$ ) and for solid-LiH, we conclude that the existing PAW potentials and the PBEsol XC functional are suitable for studying the interaction of D with liquid  $\text{Li}_{30}\text{Sn}_{70}$ .

## 2.2 Simulation cells

All KSDFT-MD simulations were performed in the canonical (constant NVT) ensemble using the Nosé-Hoover thermostat [42,43], with the SMASS-tag in VASP set to two, minimizing the fluctuations in the

total energy and temperature. A time step of 1 fs is sufficient to ensure that the total Nose-Hoover energy is conserved during the entire simulation; we sampled the plane waves only at the (0,0,0)  $k$ -point, which is appropriate for disordered systems. As liquid  $\text{Li}_{30}\text{Sn}_{70}$  does not melt congruently from any solid Li-Sn compound, we started from an already liquid  $\text{Li}_{30}\text{Sn}_{70}$  280-atom cell and randomly inserted D atoms to obtain four different concentrations corresponding to  $\beta = 7.5, 15, 22.5,$  and  $30$  in  $\text{Li}_{30}\text{Sn}_{70}\text{D}_\beta$ . All four systems were simulated at four different temperatures, namely, 670, 770, 870, and 970 K, respectively.

We followed the same procedure as in the previous study of liquid  $\text{Li}_{30}\text{Sn}_{70}$  and  $\text{Li}_{20}\text{Sn}_{80}$  to generate the simulation cells at the desired atomic densities at each temperature, where the external pressure of the simulation cell should be approximately zero [21]. An increase in the atomic density from pure  $\text{Li}_{30}\text{Sn}_{70}$  is expected due to the bonding between Li and D, as was observed for liquid  $\text{LiD}_\beta$  [25]. Once D atoms were added randomly to the liquid  $\text{Li}_{30}\text{Sn}_{70}$  280-atom cell, the system was simulated at 1500 K for 2 ps to ensure a homogeneous mixing of the D atoms in the system. Subsequently, at each of the desired temperatures, the system was simulated at the density found optimum for the pure  $\text{Li}_{30}\text{Sn}_{70}$  alloy at each temperature and at a 5% higher density. The total NVT-MD trajectories ranged from 15 to 30 ps until the pressure stabilized and the number of  $\text{D}_2$  molecules oscillated around a constant value, with the equilibrium pressure in each case obtained by sampling the last 5 ps of the trajectory. Note that the liquid alloy system takes longer equilibration times at higher  $\beta$  due to the number of  $\text{D}_2$  molecules and “bubbles” being formed (see section 3.1), which explains the range in NVT-MD equilibration times required. After calculating the equilibrium pressures, we used the two pressures and densities to linearly extra/inter-polate to a new density at which the pressure is supposedly zero. A new NVT-MD trajectory then is calculated at this new density, and, if the pressure is still non-zero, a new linear extra/inter-polation to zero pressure is performed with this density included. The process is repeated using the last two calculated pressures until the final equilibrium pressure is less than  $\pm 0.2$  GPa and the local fluctuations in pressure are  $\pm 0.4$  GPa, typically obtained after two to three pressure/density evaluations. We chose this iterative NVT-MD scheme instead of using an isobaric (NPT) ensemble since NPT simulations are more computationally expensive and require denser  $k$ -point sampling, and the pressure obtained in an NPT-MD simulation may not be the same in a subsequent NVT calculation with a different  $k$ -point mesh. Once the equilibrium atomic density (corresponding to zero external pressure) is calculated at each temperature and  $\beta$ , we simulated the systems at their equilibrium densities in NVT-MD for 40 ps to collect statistical data.

### 2.3 Liquid theory

The statistics collected from the 40 ps NVT-MD runs were used to calculate properties to obtain insight into the structural and dynamical behavior of the Li-Sn-D system.

#### 2.3.1 Static properties

We evaluated the spatial distribution of atoms by computing the partial pair distribution function,  $g_{\alpha\gamma}(r)$ , which describes the probability of finding an atom  $i$  at a distance  $r$  from another atom  $j$  [44], for atoms of species  $\alpha$  and  $\gamma$ ,

$$g_{\alpha\gamma}(r) = \frac{N}{\rho N_{\alpha} N_{\gamma}} \langle \sum_{i=1}^{N_{\alpha}} \sum_{j=1}^{N_{\gamma}} \delta(\vec{r} - \vec{R}_{ij}) \rangle, \quad (2)$$

where  $\rho$  is the atomic density,  $\delta$  is Dirac's delta function, and  $\vec{R}_{ij} = \vec{R}_i - \vec{R}_j$  where  $\vec{R}_i$  is the position of atom  $i$  as defined by its nucleus. When  $\alpha = \gamma$ ,  $i \neq j$ .

### 2.3.1 Dynamic properties

#### 2.3.1.1 Self-diffusion coefficients

We calculated the self-diffusion coefficients,  $D_s$ , of all atomic species in the liquid alloy using two different methods. First, we used the mean-squared displacement (MSD) of a tagged particle in the liquid [44] as a function of time,

$$\langle R^2 \rangle = \frac{1}{N} \sum_{j=1}^N (\vec{R}_j(t) - \vec{R}_j(0))^2, \quad (3)$$

where the self-diffusion coefficient  $D_s$  is calculated as

$$\lim_{t \rightarrow \infty} \langle R^2 \rangle = 6D_s t \quad (4)$$

with  $t$  representing the total time of the trajectory over which we average. Second, we used the velocity auto-correlation function (VACF,  $Z(t)$ ),

$$Z(t) = \frac{1}{3} \langle \vec{v}_i(t) \cdot \vec{v}_i(0) \rangle, \quad (5)$$

where  $\vec{v}_i(t)$  is the velocity vector [44] and  $D_s$  is calculated as

$$D_s = \int_0^{\infty} Z(t) dt \quad (6)$$

In addition, due to the small number of D atoms in liquid Li-Sn and in order to reduce the uncertainty associated with  $D_s$  evaluated from the MSD and VACF, we also used the self-van Hove function,  $G_s(r, t)$  [45], to calculate  $D_s$  of D-related species, i.e., free D atoms and  $D_2$  molecules, where,

$$G_s(R, t) = \langle \delta(R - |\vec{R}_i(t) - \vec{R}_i(0)|) \rangle \quad (7)$$

For particles that follow Fickian diffusion, the self-van Hove function at long distances decays as a Gaussian,

$$G_s(R, t) \propto \exp\left(-\frac{R^2}{4D_s t}\right) \quad (8)$$

We evaluated the MSD and VACF by averaging over 15 and 20 ps trajectories, taking origins every 3 fs from the full 40 ps simulation. Taking origins separated by longer periods did not give different results. We also evaluated the self-van Hove functions at 15 and 20 ps, taking origins every 3 fs.

To obtain an estimate of the D<sub>2</sub> bubbles' diffusivity formed in the system (see section 3.1), we calculated the diffusivity of the bubble referenced to the center of mass (CM) of the D<sub>2</sub> molecules. To reduce the effect of the few D<sub>2</sub> molecules that are far from the bubble CM, we first computed the CM position weighting all D<sub>2</sub> molecules equally. Subsequently, we refined the CM position by weighting the molecules differently depending on their distance to the initial CM position,  $d_{\text{CM}}$ , as follows:

$$\text{weight} = \begin{cases} 1 & \text{if } d_{\text{CM}} \leq \frac{L}{4} \\ \cos\left(\frac{\pi}{2}\left(\frac{d_{\text{CM}} - \frac{L}{4}}{L/4}\right)\right) & \text{if } \frac{L}{4} \leq d_{\text{CM}} \leq \frac{L}{2} \end{cases} \quad (9)$$

with  $L$  representing the side of the simulation box. The specific choice of the cosine weight function is to reduce the effect of the D<sub>2</sub> molecules that are far from the bubble CM faster than a linear decay. We also chose  $L/4$  as the limit of the diameter of the bubble based on snapshot observations (see section 3.1). Alternate weight functions or bubble diameter values did not have a significant effect on the final diffusivity results.

### 2.3.1.2 Shear viscosity

We calculated the shear viscosity *via* the total transverse current,  $\vec{J}_T(\mathbf{q}, t)$ , as defined by Bryk and Mryglod. [46] for a binary system, and generalized it to the case of a three-component system as

$$\vec{J}_T(\mathbf{q}, t) = \frac{1}{\sqrt{N}} \sum_{\alpha \in \{\text{Li, Sn, D}\}} \sum_{j=1}^{N_\alpha} m_\alpha v_{\alpha j}^t e^{i\vec{q} \cdot \vec{R}_{\alpha j}} \quad (10)$$

where  $N$  is the total number of atoms,  $N_\alpha$  and  $m_\alpha$  are the number of atoms and mass, respectively, of species  $\alpha$ ,  $v_{\alpha j}^t$  is the component of the velocity of particle  $j$  (of type  $\alpha$ ) transverse to the wavevector  $\vec{q}$ , and  $\vec{R}_{\alpha j}$  is the position of particle  $j$ . The transverse current correlation function,  $C_T(\mathbf{q}, t)$ , is calculated as

$$C_T(\mathbf{q}, t) = \langle \vec{J}_{\text{Li}}(\mathbf{q}, t) \vec{J}_{\text{Li}}(-\mathbf{q}, 0) \rangle + \langle \vec{J}_{\text{Sn}}(\mathbf{q}, t) \vec{J}_{\text{Sn}}(-\mathbf{q}, 0) \rangle + \langle \vec{J}_{\text{D}}(\mathbf{q}, t) \vec{J}_{\text{D}}(-\mathbf{q}, 0) \rangle + 2\langle \vec{J}_{\text{Li}}(\mathbf{q}, t) \vec{J}_{\text{Sn}}(-\mathbf{q}, 0) \rangle + 2\langle \vec{J}_{\text{Li}}(\mathbf{q}, t) \vec{J}_{\text{D}}(-\mathbf{q}, 0) \rangle + 2\langle \vec{J}_{\text{Sn}}(\mathbf{q}, t) \vec{J}_{\text{D}}(-\mathbf{q}, 0) \rangle \quad (11)$$

We used the relationship between  $C_T(\mathbf{q}, t)$  and the generalized shear viscosity,  $\tilde{\eta}(\mathbf{q}, 0)$ , obtained through the Mori-Zwanzig memory function formulation [47,48] in the generalized hydrodynamics regime,

$$\int_0^\infty \frac{c_T(q,t)}{c_T(q,0)} dt = \left[ \frac{q^2}{m\rho} \tilde{\eta}(q, 0) \right]^{-1} \quad (12)$$

where  $\rho$  is the atomic density and  $m$  is the weighted mass of the system,  $m = c_{\text{Li}}m_{\text{Li}} + c_{\text{Sn}}m_{\text{Sn}} + c_{\text{D}}m_{\text{D}}$ , with  $c$  representing a species' concentration. The shear viscosity coefficient,  $\eta$ , is obtained by extrapolating  $\tilde{\eta}(q, 0)$  to  $q \rightarrow 0$ ; we use a Lorentzian, as introduced by Balucani *et al.* [49], where  $a$  is a parameter fit to simulation data.

$$\eta(q) = \frac{\eta}{1+aq^2} \quad (13)$$

### 3. Results and discussion

Following the method described in section 2.2, we evaluate the density at  $\sim 0$  GPa for each D concentration ( $\beta$ ) in  $\text{Li}_{30}\text{Sn}_{70}$ , as plotted versus temperature in Figure 1, to simulate conditions that are similar to experiments inside a fusion reactor. We observe a decrease in mass density as  $\beta$  increases, i.e., as D is added, because of the significantly lower mass of D compared to Sn. However, the atomic density increases because of the increased tendency to form  $\text{D}_2$  molecules as  $\beta$  increases. For example, at  $\beta = 7.5$  (black triangles in Figure 1), the mass density is similar to the pure alloy (purple circles) [21], as a result of adding lighter D atoms along with a significant increase in the atom density. Notably, for  $\beta = 7.5$  and  $\beta = 15$  (red triangles), the mass density deviates away from a linearly decreasing trend as the temperature increases, with such deviations attributed to the formation of D and  $\text{D}_2$  clusters (*vide infra*). Specifically, the sharp decrease in mass density from 870 K ( $\sim 5.38 \text{ g/cm}^3$ ) to 970 K ( $\sim 5.27 \text{ g/cm}^3$ ) at  $\beta = 15$  is symptomatic of D cluster formation. Moreover, the increase in atom density with increasing D concentration influences the local trends in various properties of the liquid alloy (*vide infra*).



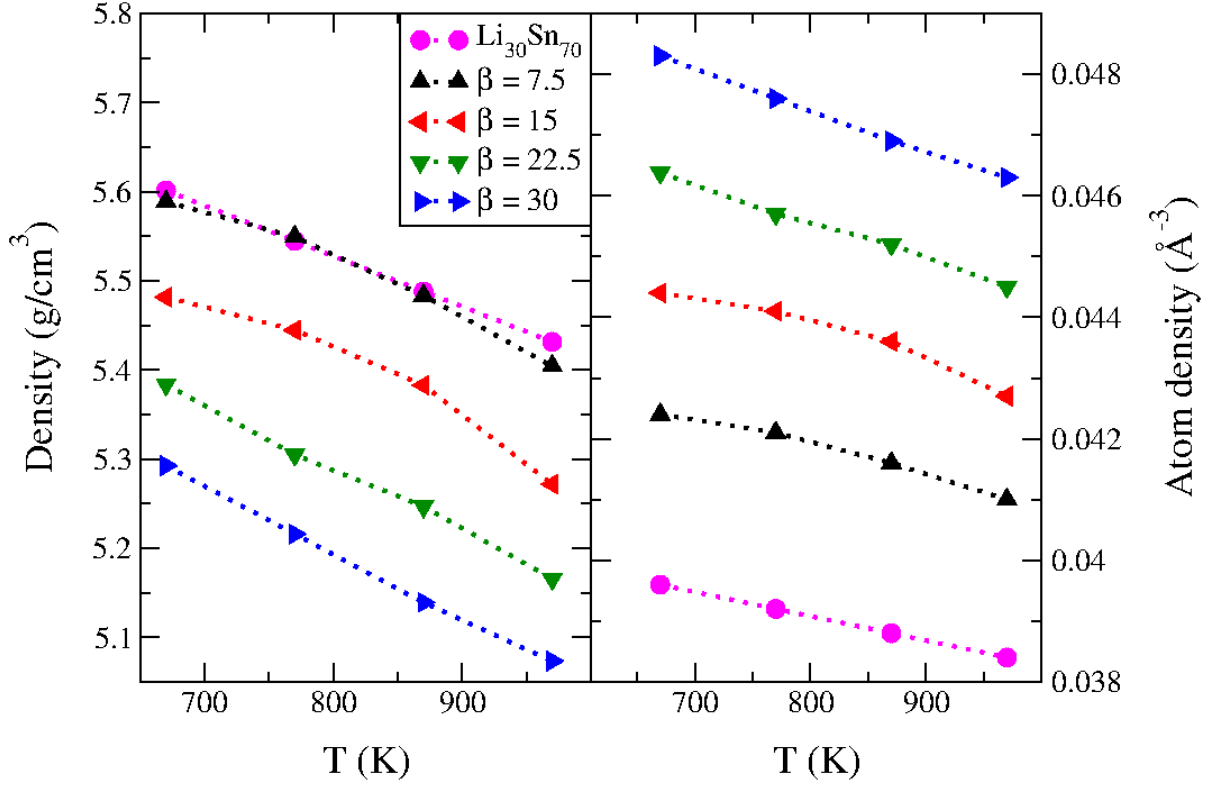


Figure 1. Calculated mass densities (left panel) and atom densities (right panel) for liquid  $\text{Li}_{30}\text{Sn}_{70}$  with four different D concentrations in  $\text{Li}_{30}\text{Sn}_{70}\text{D}_\beta$  ( $\beta = 7.5, 15, 22.5, 30$ ; solid triangles). Solid circles represent the densities predicted using similar KSDFT-MD simulations of pure liquid  $\text{Li}_{30}\text{Sn}_{70}$  from Ref 21.

### 3.1 Static structure and creation of $\text{D}_2$ molecules.

Figure 2 plots the partial pair distribution functions,  $g_{\alpha\gamma}(r)$  (section 2.3.1), amongst identical species (i.e.,  $g_{ii}(r)$ ), namely  $g_{\text{Li-Li}}(r)$  (top row),  $g_{\text{Sn-Sn}}(r)$  (middle row), and  $g_{\text{D-D}}(r)$  (bottom row), at the four different D concentrations. We include the  $g_{ii}(r)$  distributions at the lowest (670 K, solid black lines) and highest (970 K, dashed colored lines) temperatures of interest in Figure 2. As  $\beta$  and temperature increase, the  $g_{ii}(r)$  in Figure 2 vary only in the height of the first and second peaks, but not on the number or location of the peaks. Importantly, the overall shape of  $g_{\text{Li-Li}}(r)$  and  $g_{\text{Sn-Sn}}(r)$  are similar to the pure  $\text{Li}_{30}\text{Sn}_{70}$  alloy [21], which remains in the liquid state across 670-970 K.  $\text{Li}_{30}\text{Sn}_{70}\text{D}_\beta$  therefore does not crystallize across the range of temperatures and  $\beta$  studied in this work. In contrast, a KSDFT-MD simulation of liquid Li with D inserted at various concentrations, i.e.,  $\text{LiD}_\beta$ , predicted that the crystallization temperature of the Li-D system increases with  $\beta$ , up to around 900 K for  $\beta=1$  [25], due to the appearance of additional peaks in  $g_{\text{Li-Li}}(r)$  between 3 and 5 Å. While crystallization in the binary Li-D liquid can be attributed to the high melting

point of LiD ( $965 \pm 2$  K [50]) our data indicate importantly that alloying Li with Sn can suppress solidification caused by D addition.

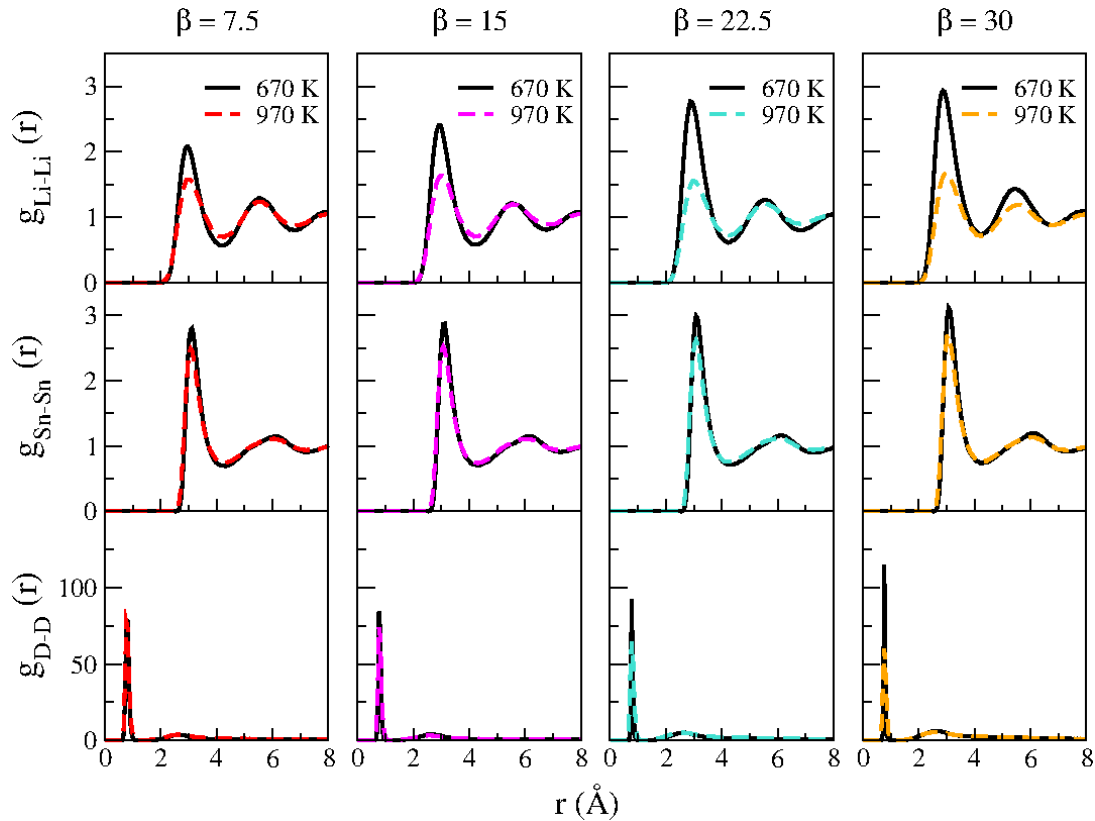


Figure 2. Partial pair distribution functions,  $g_{ii}$ , from KSDFT-MD simulations for the different species in the liquid  $\text{Li}_{30}\text{Sn}_{70}\text{D}_\beta$  alloy: Li-Li (upper row), Sn-Sn (middle row), and D-D (lower row). We simulate  $\beta$  ranging from 7.5 (left column) to 30 (right column), while solid black and dashed colored curves indicate 670 K and 970 K, respectively.  $g(r)$  is normalized with respect to the average atom density of the species within the overall liquid. Thus, large values of  $g_{\text{D-D}}(r)$ , versus  $g_{\text{Li-Li}}(r)$  or  $g_{\text{Sn-Sn}}(r)$ , indicate a significantly higher probability of finding a D atom at a distance similar to a  $\text{D}_2$  gas molecule, as compared to the probability of finding atoms at similar distances in the overall liquid alloy.

Another important distinction from the binary  $\text{LiD}_\beta$  system is that the  $g_{\text{D-D}}(r)$  in  $\text{Li}_{30}\text{Sn}_{70}\text{D}_\beta$  exhibits a sharp peak at  $\sim 0.78$  Å (bottom row in Figure 2), similar to the D-D bond length in a  $\text{D}_2$  molecule, signifying the presence of  $\text{D}_2$  molecules. Note that pure liquid Li instead retains a high concentration of D atoms and forms Li-D bonds [25]. Hence, the formation of  $\text{D}_2$  molecules in  $\text{Li}_{30}\text{Sn}_{70}\text{D}_\beta$  indicates that alloying Sn reduces the Li-D affinity, consistent with measured thermodynamic data (see section 3.2 below). It therefore is more favorable energetically for D to form  $\text{D}_2$  molecules than to bond with Li or Sn in the  $\text{Li}_{30}\text{Sn}_{70}$  alloy.

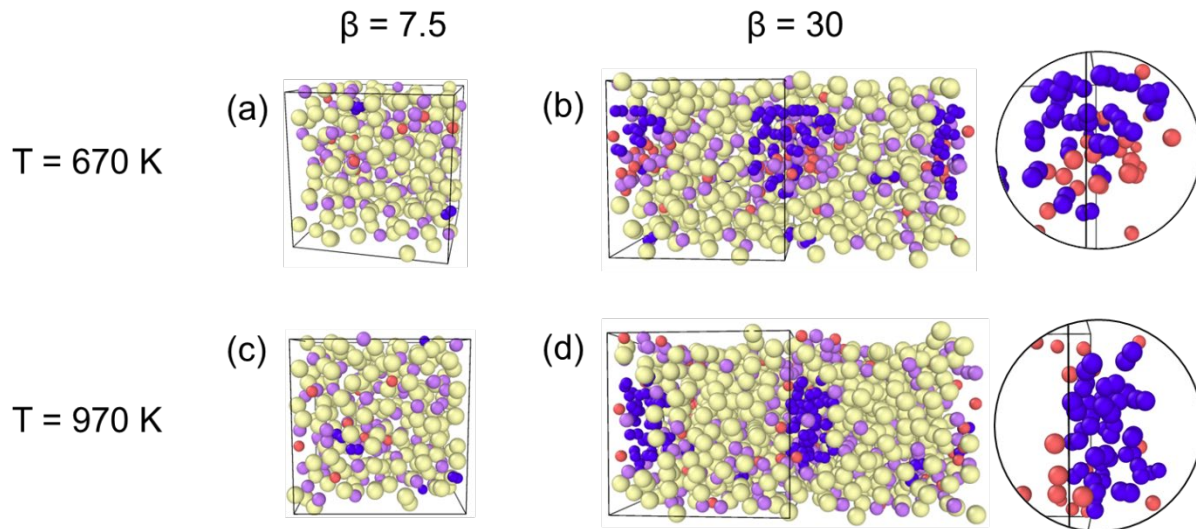


Figure 3. Three-dimensional snapshots of liquid  $\text{Li}_{30}\text{Sn}_{70}\text{D}_\beta$  samples with D concentrations of  $\beta = 7.5$  and  $\beta = 30$ , at 25 ps after equilibration. Li atoms depicted in purple, Sn atoms in yellow, free D atoms in red, and  $\text{D}_2$  molecules in blue. Snapshots shown for the minimum and maximum temperatures simulated. Snapshots (b) and (d) exhibit the D atoms in a bubble-like arrangement, showing two neighboring periodic cells, surrounded by a higher concentration of Li atoms than in the rest of the liquid alloy. Circular images in (b) and (d) are expanded images of the central bubble in the snapshots, where only D and  $\text{D}_2$  are depicted.

To visualize the addition of D in liquid  $\text{Li}_{30}\text{Sn}_{70}$ , we display snapshots of the KSDFT-MD simulations of  $\text{Li}_{30}\text{Sn}_{70}\text{D}_\beta$  for  $\beta = 7.5$  (panels a and c) and  $\beta = 30$  (panels b and d) at temperatures of 670 K (top row) and 970 K (bottom row) in Figure 3. The insets of panels b and d in Figure 3 distinguish between free D atoms (red) and D atoms forming a  $\text{D}_2$  molecule (blue); the Li and Sn atoms in the insets are not shown for clarity. D atoms start to cluster at high  $\beta$  ( $= 30$ ), forming  $\text{D}_2$  molecules that coalesce eventually to form gas bubbles (Figure 3 (b) and (d)), while  $\text{D}_2$  clustering is not significant at low  $\beta$  ( $= 7.5$ ). These bubbles primarily consist of  $\text{D}_2$  molecules, surrounded by a small amount of free D atoms and Li atoms that segregate towards the bubble from the liquid alloy. Li segregation to the surface of the  $\text{D}_2$  bubble is not surprising: Li typically segregates towards the liquid surface in Li-Sn alloys due to its lower surface tension [19–21]. In this case, Li atoms segregate to the liquid surface in contact with the  $\text{D}_2$  gas bubble.

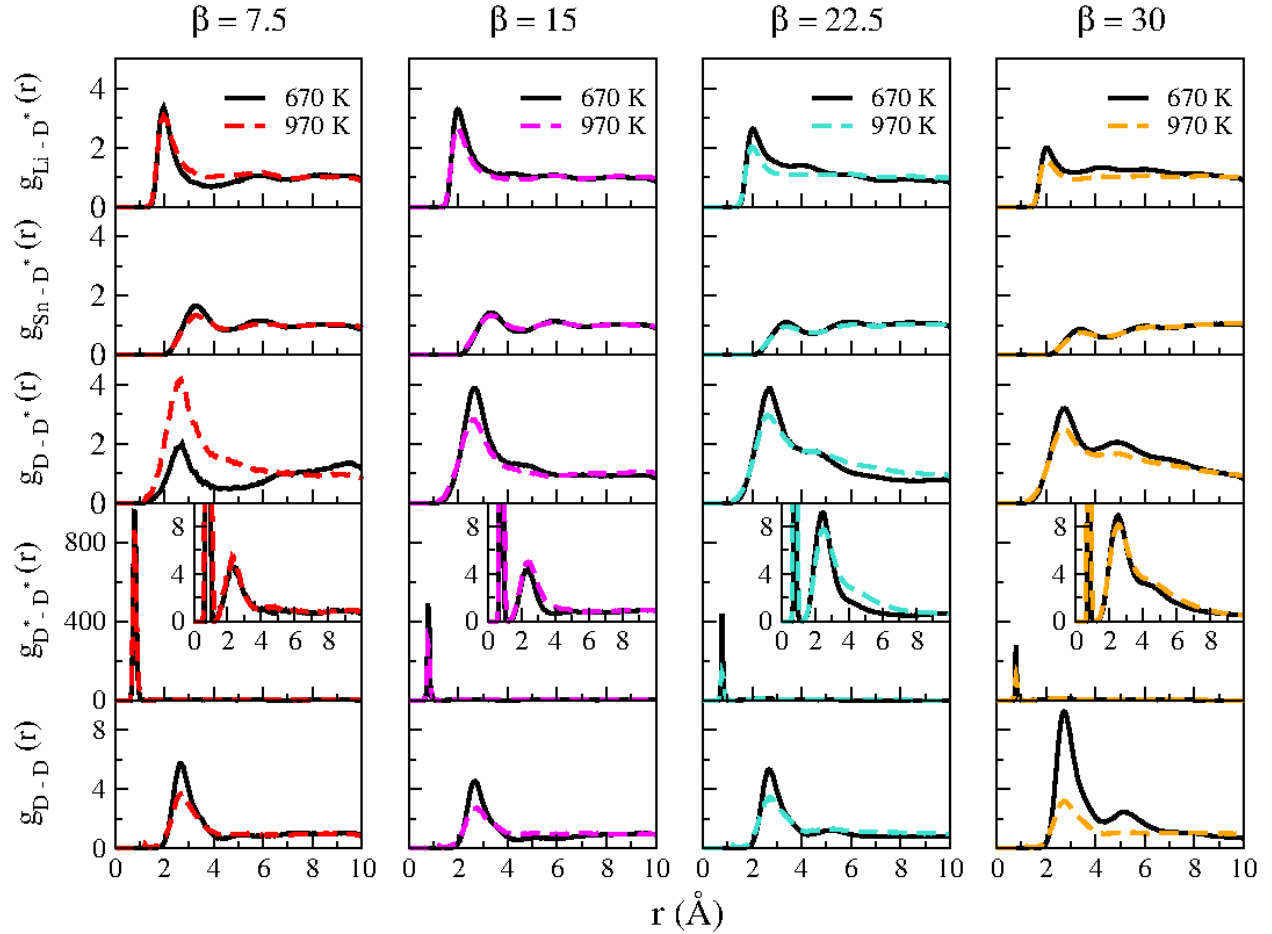


Figure 4. Partial pair distribution functions,  $g_{ij}$ , at each D concentration in the liquid alloy  $\text{Li}_{30}\text{Sn}_{70}\text{D}_\beta$  with respect to  $\text{D}^*$  with: Li (first row), Sn (second row), free D (third row), and  $\text{D}^*$  (fourth row).  $\text{D}^*$  refers to D atoms that form  $\text{D}_2$  molecules, where the inset of  $g_{\text{D}^*-\text{D}^*}$  shows a close up of the intermediate range order between  $\text{D}^*$  atoms. The fifth row represents the partial pair distribution function of pairs of free D atoms. Black/solid curves at 670 K; color/dashed curves at 970 K.

Due to the formation of  $\text{D}_2$  bubbles and Li segregation, we analyzed the arrangement of Li, Sn, and D with respect to D in  $\text{D}_2$  molecules by studying their respective  $g_{\alpha\gamma}(r)$  at different  $\beta$  and temperatures, as plotted in Figure 4. For the calculation of the different pair distribution functions, we distinguished between free D atoms (labeled “D” in Figure 4) and D atoms that form  $\text{D}_2$  molecules (labeled  $\text{D}^*$ ) at each time step. Notably, the probability of Li atoms having a  $\text{D}^*$  as a neighbor (top row, Figure 4) decays with increasing D concentration, especially for  $\beta \geq 22.5$ . Similarly, the probability of Sn atoms having  $\text{D}^*$  as a neighbor ( $g_{\text{Sn}-\text{D}^*}$ , second row in Figure 4) decays with increasing  $\beta$  and remains significantly lower than  $g_{\text{Li}-\text{D}^*}$  across all  $\beta$  and temperatures. The decay in both  $g_{\text{Li}-\text{D}^*}$  and  $g_{\text{Sn}-\text{D}^*}$  with increasing  $\beta$  can be attributed to the formation of  $\text{D}_2$  bubbles (Figure 3(b) and (d)), which attracts  $\text{D}^*$  away from the vicinity of Li or Sn. Also, the surface

of the  $D_2$  bubbles exhibits segregated Li atoms (Figure 3 (b) and (d)), signifying fewer  $D^*$  neighbors for Sn than Li as  $D_2$  bubbles form.

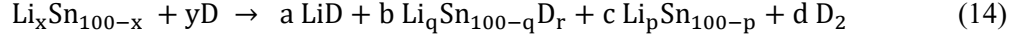
With respect to the local arrangement of D atoms,  $g_{D-D^*}$  at  $\beta = 7.5$  exhibits a low probability for  $D$ - $D^*$  nearest neighbors at 670 K (Figure 4, middle row) because of the low number of  $D_2$  molecules formed (Figure 3 (a)). As  $\beta$  increases, free D atoms increasingly exhibit  $D^*$  atoms as neighbors since  $D_2$  molecules exhibit clustering (and eventually bubble formation), which attracts free D towards  $D^*$ . In the fourth row of Figure 4,  $g_{D^*-D^*}$  presents a sharp peak (at  $\sim 0.78$  Å), indicative of the formation of  $D_2$  molecules, across  $\beta$  and temperatures. The insets within  $g_{D^*-D^*}$  depict a close-up on the intermediate range order (for  $r$  larger than the  $D^*-D^*$  bond length in  $D_2$ ) between  $D^*$  atoms. Once the  $D_2$  clusters are large enough ( $\beta = 22.5$  and 30 in Figure 4) and bubbles form (Figure 3 (b) and (d)), an intermediate range order appears in  $g_{D^*-D^*}$ , as signified by a peak at  $r \sim 2.7$  Å and the appearance of a side shoulder. Finally, free D atoms have a higher probability of being surrounded by other free D atoms ( $g_{D-D}$ ) once the  $D_2$  bubbles form at 670 K, as seen for  $\beta = 30$  in the bottom row of Figure 4. This is because free D atoms segregate towards the  $D_2$  bubble and, as a result, the movement of free D is confined to the bubble surface (Figure 3(b)). Importantly, as the temperature increases, free D can exhibit enough kinetic energy to overcome segregation towards the  $D_2$  bubble and can move freely through the liquid alloy (Figure 3 (d)), as evident from a significant reduction in  $g_{D-D}$ , at  $\beta = 30$ , from 670 K to 970 K.

Combining the data from Figures 2 and 4, it is evident that formation of  $D_2$  molecules and Li segregation towards  $D_2$  clusters readily occurs. Together with the lack of bonding between Sn and D, these observations point to low D retention since the gas molecules eventually will desorb from the liquid. Interestingly, the D retention is much lower than what would be expected from the amount of Li atoms in the system, given the 1:1 affinity between Li and D in pure liquid Li [25,27,51,52]. Thus, the presence of Sn strongly perturbs the liquid metal and is directly responsible for the low D retention in liquid  $Li_{30}Sn_{70}D_\beta$ . As the retention of fuel is not a desirable property, this Li-Sn alloy is a favorable PFC candidate.

### *3.2 Thermodynamic study of $D_2$ formation in liquid Li-Sn alloys*

The reduction in the D retention of liquid Li-Sn as the concentration of Sn increases is important to quantify, as the Li concentration will vary along the liquid  $Li_{30}Sn_{70}$  surface due to Li segregation. The extent of Li segregation to the liquid surface of  $Li_{30}Sn_{70}$  is unclear, with theoretical and experimental studies providing a wide range from  $\sim 40$  % to  $\sim 100$  % segregation [19–21]. Additionally, calculating the extent of the  $D_2$  retention using KSDFT-MD simulations for different Li-Sn alloys concentrations carries a significant computational expense. We therefore used thermodynamic sub-lattice models [40] and the Sievert's constant [53] obtained from experimental data [54] to estimate the solubility limit of D as a function of the alloy concentration ( $x$  in  $Li_xSn_{100-x}$ ). We specifically estimate the concentration of Li-rich Li-Sn at which

Li's retention of D starts to diminish and D atoms form  $D_2$  molecules. We use a convex hull optimizer [55], where we minimize the Gibbs energy of Eq. 14 and identify the products at equilibrium for a given temperature (T), initial alloy concentration (x), and  $D_2$  addition (y):



Eq. 14 considers the potential formation of binary LiD, binary  $Li_pSn_{100-p}$ , ternary  $Li_qSn_{100-q}D_r$  (where p, q can be different from x), and  $D_2$  molecules at their corresponding molar fractions a, b, c, and d, respectively. We used data from a thermodynamic sub-lattice model [40] to determine the Gibbs energies of liquid (and solid) binary Li-Sn alloys. The experimental data used for  $D_2$  is the same as for  $H_2$ , since the enthalpic differences between D- and H-compounds are negligible [41,56]. Similarly, the data used for liquid and solid LiD is the same as the experimental data for LiH [41,57]. To ensure that the D solubility within liquid Sn is zero under the temperatures of study here, in line with experimental observations of negligible D solubility in Sn [12], we used a simple regular solution model for liquid Sn-D (i.e., Sn-H), where Sn-D interactions are penalized energetically ( $\sim 40$  kJ per Sn-D bond). We used a Muggianu weighted sum [58] of binary Li-Sn, Li-D, and Sn-D liquid Gibbs energies to obtain the Gibbs energy of ternary Li-Sn-D liquid, since experimental measurements are scarce and thermodynamic models do not exist for the ternary system. Finally, to estimate quantitatively the low D solubility in the ternary Li-Sn-D system (i.e., under scenarios where  $r < 0.001$  in  $Li_qSn_{100-q}D_r$ ), we used the Sievert's constant [53] obtained from experimental observations of two specific Li-Sn compositions,  $Li_{57}Sn_{43}$  and  $Li_{62}Sn_{38}$  [54].

Figure 5 plots the percentage of added D that forms  $D_2$  gas (i.e.,  $\frac{d}{y}$  in Eq. 14) for different Li-rich ( $x > 80$ ) Li-Sn alloy concentrations at a temperature of 1050 K, where  $Li_xSn_{100-x}$  remains in the liquid state for  $0 \leq x \leq 100$ . Blue (red) regions in Figure 5 indicate large (small) proportions of  $D_2$  gas formation in the liquid. In general, higher (lower) Li content favors D retention ( $D_2$  gas formation) in  $Li_xSn_{100-x}$ . Importantly, there exists a limiting Li concentration,  $x_{\text{limiting}} \sim 82\%$ , below which virtually no D atom is retained in the liquid across all values of y in Eq. 14, i.e., all added D forms  $D_2$  molecules within the liquid. The existence of  $x_{\text{limiting}}$  indicates the higher driving force to form Li-Sn and D-D bonds over Li-D bonds. Additionally,  $x_{\text{limiting}}$  (i.e.,  $Li_{82}Sn_{18}$ ) is similar to the concentration of Li in  $Li_7Sn_2$ , the Li-Sn intermetallic compound with the highest experimental melting point [40].  $Li_7Sn_2$  therefore signifies the "ideal" coordination or clustering environment for the Li-Sn system. The 'free' Li atoms at Li concentrations higher than  $Li_7Sn_2$ , i.e., Li atoms not bonded to Sn within a  $Li_7Sn_2$  configuration, will bond eventually to a D atom and contribute to D retention within the liquid alloy.

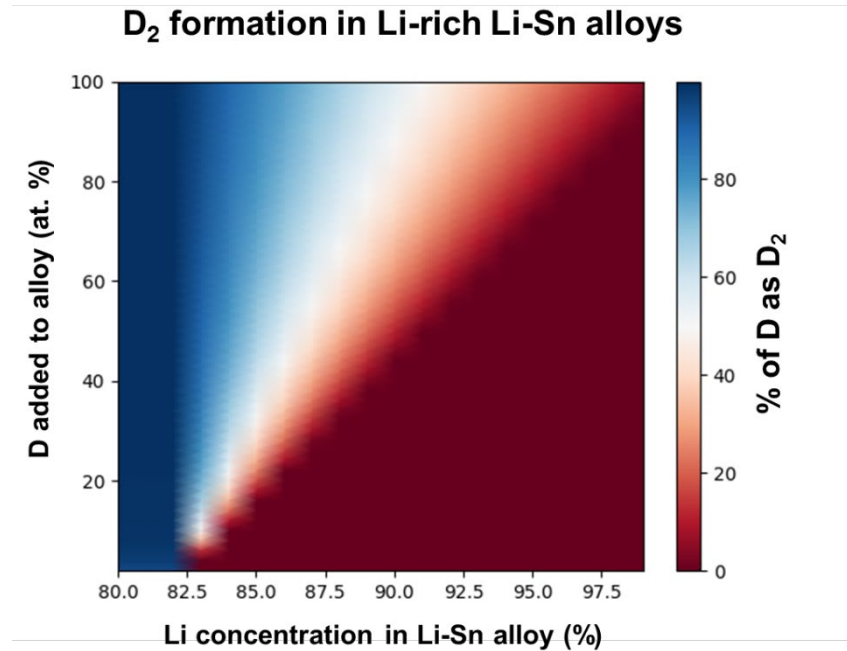


Figure 5. Amount of  $D_2$  gas formed (in % with respect to the total D added) in Li-rich Li-Sn alloys. Red (blue) indicates high (low) D retention. For Li-Sn alloys with a Li concentration lower than 82 %, practically all D added to the alloy will form  $D_2$  molecules. Results are for a temperature of 1050 K, higher than any melting temperature in the Li-Sn and Li-D phase diagrams to avoid solidification of any resulting compound.

Based on data from Figure 5, we do not expect to have any free D atoms in our liquid  $Li_{30}Sn_{70}$  system, i.e., D atoms form  $D_2$  molecules and evolve out of the liquid. However, the KSDFT-MD snapshots in Figure 3 do indicate the presence of free D atoms within liquid Li-Sn. One reason for this discrepancy may be the necessarily finite simulation time, which may not be long enough for all the D atoms to find each other and form  $D_2$ . However, as mentioned in Section 2.2, during the 40 ps production run, the number of  $D_2$  molecules in the system is approximately constant, different from the continuous increase in  $D_2$  molecule formation observed in the equilibration run (first 15-30 ps). Therefore, the presence of free D atoms within the liquid may not be a finite-time artifact but could also be due to the different conditions under which the experiment and simulations are performed. For example, there is no vacuum (or gaseous phase) available for the  $D_2$  molecule to occupy by escaping the liquid alloy in the KSDFT-MD simulations. Therefore, the formation and existence of  $D_2$  molecules (and bubbles) in the liquid alloy has an energetic cost, namely, the interfacial energy of the gas/bubble with the liquid molecules/surface. This enforces a dynamic equilibrium between i) the number of free  $D_2$  molecules formed, ii) the number of  $D_2$  molecules that cluster together eventually to form bubbles (at high  $\beta$ ), and iii) free D atoms that remain dissolved in the liquid alloy. In the case of experiments, all thermodynamic data are obtained from (quasi-)equilibrium measurements, where the  $D_2$  molecules formed within the liquid alloy are provided sufficient time to escape into the gas

phase/vacuum region surrounding the liquid. Nevertheless, the conditions of our KSDFT-MD simulations are representative of the liquid surface's interior being bombarded by the plasma particles (such as D). Upon reaching deep regions within the liquid surface, a dynamic equilibrium will be established between  $D_2$  molecules formed and the free D atoms within the liquid. Eventually, the  $D_2$  molecules (or bubbles) should diffuse to the surface and escape, lowering the overall D concentration in the liquid. Thus, given a constant rate of plasma bombardment and the diffusion of  $D_2$  molecules (or bubbles), which sets the overall D concentration, there always will be a non-negligible amount of free D atoms in the liquid film. Our MD simulations predicting non-negligible D retention in liquid Li-Sn therefore should resemble closely the operating conditions in a fusion reactor.

### 3.3 Diffusivity

Figure 6 quantifies the diffusivity of various species within  $Li_{30}Sn_{70}D_{\beta}$ , including free D atoms and  $D^*$  atoms that form  $D_2$  molecules at various  $\beta$  and temperatures. Note that the overall D concentration in the Li-Sn PFC will depend on the rate of D bombardment, along with the diffusivity of D atoms,  $D_2$  molecules, and  $D_2$  bubbles (Figure 7, *vide infra*) in the liquid. Additionally, we consider only the diffusion of the CM for each  $D_2$  molecule to eliminate the vibrational and rotational effects within all  $D_2$  molecules. As diffusivity is a dynamic property, the forming and breaking of  $D_2$  molecules during the MD simulation can greatly affect the corresponding diffusivity estimates for free D and  $D^*$ . Hence, we differentiate free D and  $D^*$  atoms based on the following criteria: i) free D atoms are those that remain free (i.e., do not form  $D_2$ ) for more than 35 ps (out of the total 40 ps) of the MD simulation, ii) only  $D_2$  molecules that do not break up during the entire simulation are labeled  $D^*$ , and iii) D atoms that do not fall into either of the two previous categories are not considered for diffusivity estimates.



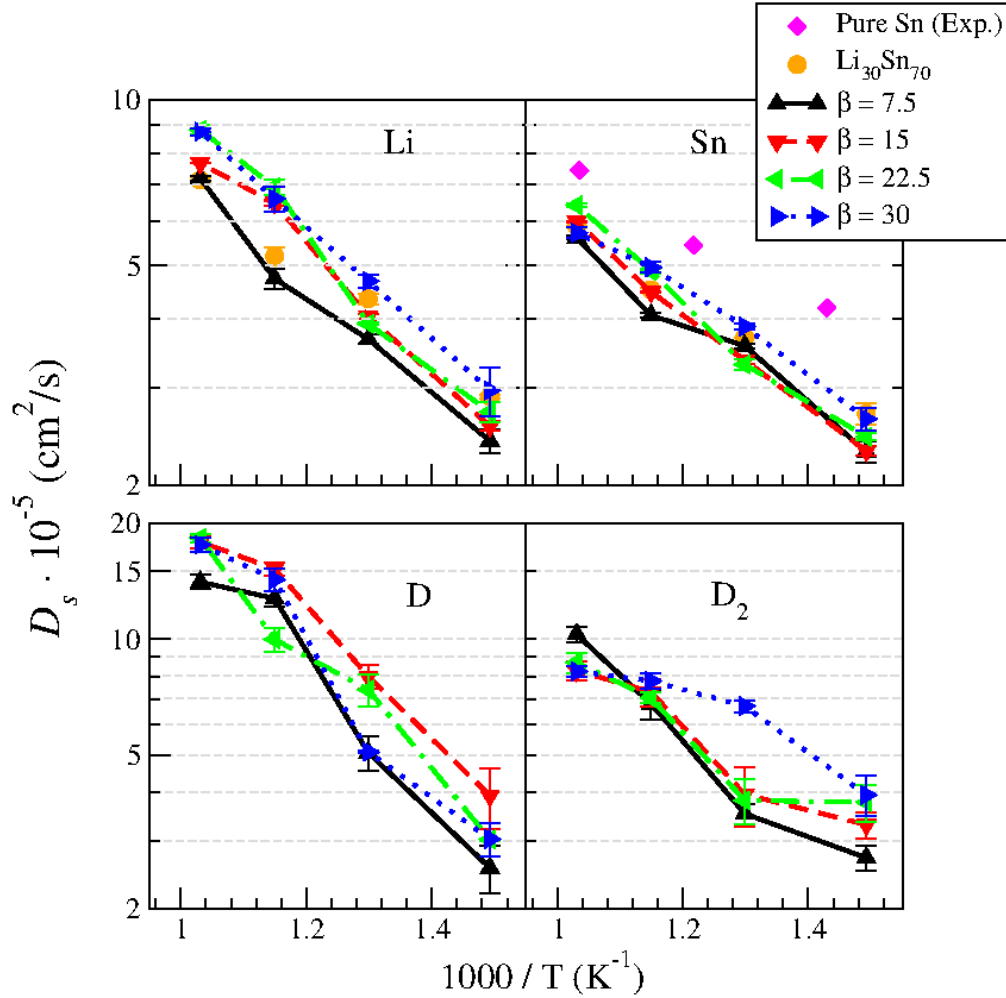


Figure 6. Self-diffusion coefficients from KSDFT-MD of Li (upper left), Sn (upper right), D free atoms (lower left), and  $D_2$  molecules (lower right) for each D concentration:  $\beta = 7.5$  (black up triangles),  $\beta = 15$  (red down triangles),  $\beta = 22.5$  (green left triangles), and  $\beta = 30$  (blue right triangles). Self-diffusion coefficients from KSDFT-MD of Li and Sn atoms in the pure  $Li_{30}Sn_{70}$  alloy (orange dots) are from Ref. 21. Experimental data for pure liquid Sn (pink diamonds) are from Ref. 59. Error bars are derived from evaluating the diffusion coefficients by the methods described in section 2.3.

The diffusivity of Li (upper left panel in Figure 6) displays a non-monotonic trend with variations in  $\beta$ . For example, at  $\beta = 7.5$ , the Li diffusivity is lower than for pure  $Li_{30}Sn_{70}$  across all temperatures, possibly due to a higher atom density in the alloy (Figure 1), while Li diffusivity is higher than pure  $Li_{30}Sn_{70}$  at higher  $\beta$ . Although the atom density increases as  $\beta$  increases, D atoms exhibit clustering, which drives Li segregation and creates free space for the movement of Li (and Sn) atoms. In contrast to Li, Sn diffusivity (upper right panel) exhibits a smaller variance with respect to diffusivity in  $Li_{30}Sn_{70}$  due to a lack of affinity

with D. Thus, variations in Sn diffusivity as  $\beta$  increases are largely due to a combination of increased atom density and the clustering of D atoms away from Sn atoms.

Similar to Li, diffusivity of free D atoms also exhibits a strong non-monotonic trend with  $\beta$  across temperatures (lower left panel in Figure 6). At low D concentrations ( $\beta$  from 7.5 to 15), the diffusivity increases due to the clustering of  $D_2$ , which creates a concentration gradient for free D atoms and subsequently drives the diffusion of D towards the  $D_2$  cluster. As  $\beta$  increases (from 15 to 22.5 and 30), the diffusivity decreases due to the creation of  $D_2$  bubbles where D atoms preferentially locate at the surface of such bubbles, restricting the movement of D atoms and lowering their diffusivity. As the temperature is increased at high  $\beta$  (22.5 and 30), the coherence of the bubble diminishes and free D atoms diffuse more freely within the liquid. Analogous to free D, the diffusion of  $D_2$  molecules increases as  $\beta$  increases from 7.5 to 15, across temperatures, due to the clustering of  $D_2$  (lower right panel in Figure 6). The diffusivity increases when  $\beta$  increases from 15 to 22.5 and 30, but only at low temperatures (670-770 K). The formation of bubbles at high  $\beta$  (22.5 and 30) indicates that  $D_2$  molecules have more freedom to move inside the bubble than the rest of the Li-Sn liquid, resulting in higher diffusivities compared to lower  $\beta$  (7.5 and 15) at lower temperatures. However, the bubble coherence reduces as the temperature increases (870-970 K), i.e.,  $D_2$  bubbles tend to break up into smaller clusters. This leaves isolated  $D_2$  molecules to diffuse through the Li-Sn liquid, i.e.,  $D_2$  molecules diffuse through regions of higher gravimetric density liquid than inside the bubble, resulting in a reduced diffusivity.

Figure 7 shows the diffusivity of the  $D_2$  bubble within the Li-Sn liquid at  $\beta = 30$ , calculated through the method described in section 2.3.1, where we only consider the weighted CM of all  $D_2$  molecules as specified in Eq. 9. Similar to trends for Li and Sn atoms (Figure 6), the diffusivity of the  $D_2$  bubble increases with increasing temperature. However, the  $D_2$  bubble will diffuse more slowly ( $\sim$ one order of magnitude smaller diffusivity) compared to free D or  $D_2$  molecules (Figure 6) in liquid Li-Sn. Thus, free D and  $D_2$  molecules will diffuse twice as fast as Li and Sn only until  $D_2$  molecules cluster and form bubbles. Subsequently, the low diffusivity of the bubble will cause a slow release of D from liquid  $Li_{30}Sn_{70}$ . For a low D bombardment rate at the liquid surface, the D concentration in liquid  $Li_{30}Sn_{70}$  will remain low enough to avoid the formation of  $D_2$  bubbles in the system. However, if the D bombardment rate is high enough, then the D concentration in the liquid will reach levels where  $D_2$  bubbles will form. For high bombardment rates, the escape of  $D_2$  bubbles, which might increase the sputtering of alloy atoms into the plasma, could be a concern for the use of Li-Sn as a PFC. Isolated  $D_2$  molecule desorption, at a lower D bombardment, will be less harmful to the plasma *vis-à-vis* sputtering.

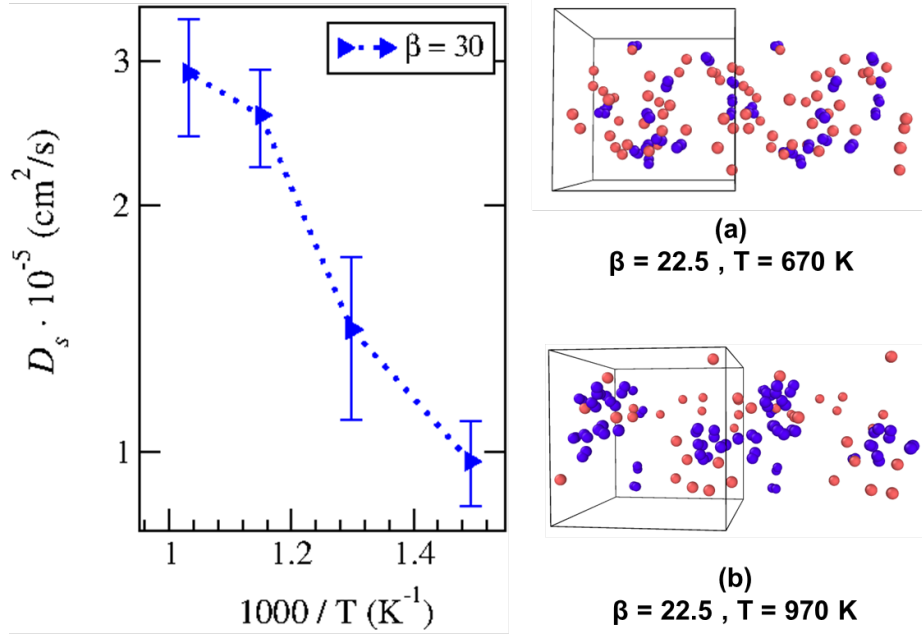


Figure 7. Self-diffusion coefficients of the  $\text{D}_2$  bubble calculated as the diffusion of the CM for all of the  $\text{D}_2$  molecules.  $\beta = 7.5$  and  $15$  are not considered as no bubbles are formed. For  $\beta = 22.5$ , the large dispersion of the  $\text{D}_2$  molecules (see (a) and (b)) introduce significant noise and error into the calculations and also are not considered. Free D free atoms are red, and  $\text{D}_2$  molecules are blue. Two neighboring periodic cells are shown.

### 3.4 Viscosity

Figure 8 displays the shear viscosity calculated for pure liquid  $\text{Li}_{30}\text{Sn}_{70}$ ,  $\text{Li}_{30}\text{Sn}_{70}\text{D}_\beta$  at  $\beta=7.5, 15$ , and  $\text{LiD}_\beta$  at  $\beta=0.25$  using the framework described in section 2.3.1 and Eqs. 10-13. The KSDFT-MD simulation data used for the viscosity calculation of  $\text{Li}_{30}\text{Sn}_{70}$  were taken from Ref. 21 and for the viscosity of  $\text{LiD}_\beta$  at  $\beta=0.25$  from Ref. 25. Notably, the viscosity for pure liquid  $\text{Li}_{30}\text{Sn}_{70}$  is higher compared to experimental viscosities of pure liquid Li and liquid Sn [60,61], in accordance with the decrease in the self-diffusion coefficients reported in Figure 6. Surprisingly,  $\text{LiD}_\beta$  ( $\beta = 0.25$ ) exhibits a significantly higher viscosity than pure liquid Li, despite  $\text{LiD}_\beta$  remaining in the liquid state (i.e., no spurious solidification [25]) under the range of temperatures considered. Hence, the higher viscosity of  $\text{LiD}_\beta$  is predominantly due to Li-D interactions (and bonding); indeed the larger increases in viscosity for  $\text{LiD}_\beta$  with decreasing temperature could be ascribed to formation of some solid LiD nuclei within the liquid.

Analogous to  $\text{LiD}_\beta$  versus Li, a higher viscosity is also observed in  $\text{Li}_{30}\text{Sn}_{70}\text{D}_\beta$  with  $\beta = 7.5$  and  $15$ , than the pure  $\text{Li}_{30}\text{Sn}_{70}$  alloy ( $\beta = 0$ ), by a factor of 6. Similar to  $\text{LiD}_\beta$  ( $\beta = 0.25$ ), the higher viscosity in  $\text{Li}_{30}\text{Sn}_{70}\text{D}_\beta$  may be related to the bonding of Li to D (apart from the increase in atom density), which would

result in a viscosity increase that is proportional to the concentration of retained D. Moreover, the concentration of D retained does not vary significantly between  $\beta = 7.5$  and 15 (Figures 3 and 5), explaining the lack of viscosity variation between the two  $\beta$  values. Note also that the relative increase in viscosity in  $\text{Li}_{30}\text{Sn}_{70}\text{D}_\beta$  versus pure  $\text{Li}_{30}\text{Sn}_{70}$  (< one order of magnitude) is not as high as for  $\text{LiD}_\beta$  ( $\beta = 0.25$ ) versus pure Li (~a factor of 10), which can be attributed to a smaller proportion of retained D in  $\text{Li}_{30}\text{Sn}_{70}\text{D}_\beta$  than in  $\text{LiD}_\beta$  ( $\beta = 0.25$ ) and the formation of solid nuclei in the latter. Nevertheless, an increase in viscosity of liquid  $\text{Li}_{30}\text{Sn}_{70}\text{D}_\beta$  will affect the type of mechanism considered for utilizing the liquid PFC, such as a flowing liquid metal or using a porous mesh. In any case, since the viscosity in  $\text{Li}_{30}\text{Sn}_{70}\text{D}_\beta$  is similar in magnitude to that of  $\text{LiD}_\beta$  ( $\beta = 0.25$ ), we expect successful mechanisms implemented for liquid Li to also perform efficiently for  $\text{Li}_{30}\text{Sn}_{70}$ .

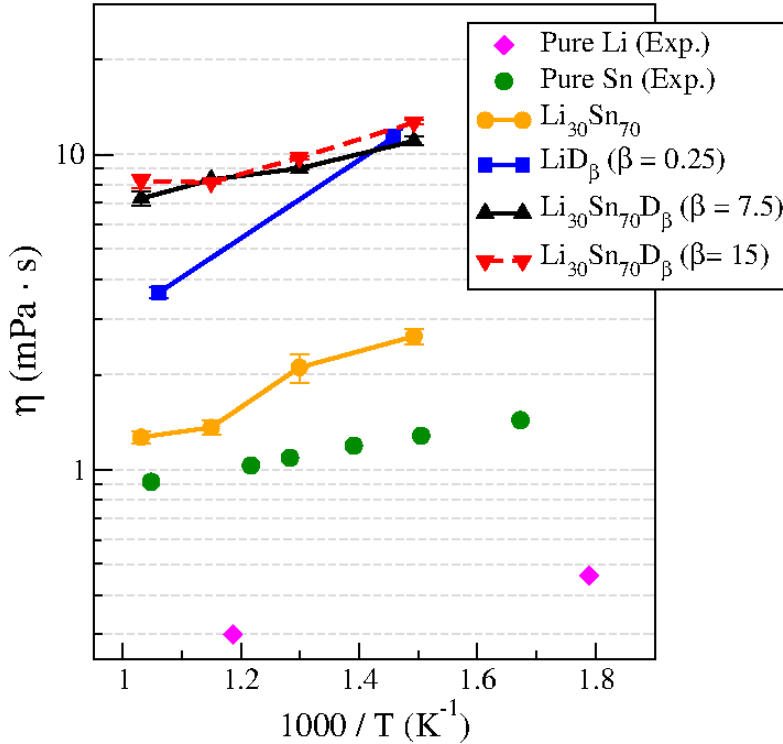


Figure 8. Shear viscosities of pure liquid  $\text{Li}_{30}\text{Sn}_{70}$  (orange dots),  $\text{Li}_{30}\text{Sn}_{70}\text{D}_\beta$  at  $\beta = 7.5, 15$  (solid triangles), and  $\text{LiD}_\beta$  at  $\beta = 0.25$  (squares). The KSDFT-MD simulation data used for the viscosity calculation of  $\text{Li}_{30}\text{Sn}_{70}$  were taken from Ref. 21 and for the viscosity of  $\text{LiD}_\beta$  at  $\beta = 0.25$  from Ref. 25. Experimental data for pure liquid Li (pink diamonds) [60] and pure liquid Sn (green dots) [61] are included for comparison. Shear viscosities for  $\beta = 22.5$  and 30 are not included, as the method used for their calculation is only valid for homogeneous liquids and therefore not compatible with the presence of gas bubbles.

#### 4. Summary and Conclusions

We performed a KSDFT-MD study of static and dynamic properties of liquid  $\text{Li}_{130}\text{Sn}_{70}\text{D}_\beta$  at different temperatures (670-970 K) and  $\beta$  (7.5-30), and analyzed implications for the potential use of liquid  $\text{Li}_{130}\text{Sn}_{70}$  as a PFC in nuclear fusion reactors. After calculating the equilibrium mass and atom densities at 0 GPa for each temperature- $\beta$  combination (Figure 1), we then studied local atomic distributions by computing partial pair distribution functions,  $g_{\alpha\gamma}(r)$  (Figures 2 and 4) and visually examining snapshots of the simulations (Figure 3). We observed that  $\text{Li}_{130}\text{Sn}_{70}\text{D}_\beta$  does not crystallize in our MD simulations within the temperature range of interest; this is contrary to liquid  $\text{LiD}_\beta$  [25], which can crystallize into solid  $\text{LiD}$ . Notably, we found that Sn does not interact strongly with D, as indicated by the considerably lower  $g_{\text{Sn-D}^*}(r)$  values than  $g_{\text{Sn-Li}}(r)$  or  $g_{\text{Li-D}^*}(r)$ , consistent with the measured low D solubility in liquid Sn [12]. Sn's presence also decreases the affinity of Li to form Li-D bonds, resulting in  $\text{D}_2$  molecule formation in the liquid. Eventually, at high  $\beta$  (22.5-30), these  $\text{D}_2$  molecules cluster and form gas bubbles within the liquid. The formation of these bubbles causes the segregation of both D and Li, where free D atoms, along with Li atoms, accumulate at the bubble surface.

To further quantify the D retention in liquid Li-Sn alloys, we performed a thermodynamic study of the ternary Li-Sn-D system (Figure 5), indicating that D can be retained only in Li-rich composition regions ( $x > 82$  in  $\text{Li}_x\text{Sn}_{100-x}$ ) of the liquid Li-Sn system. While  $\text{D}_2$  molecules are favored thermodynamically to form within the regions of higher Sn concentration ( $x < 82$ ), the retention of D for  $x > 82$  is directly related to the amount of Li atoms that remain “free” beyond a  $\text{Li}_7\text{Sn}_2$  configuration, the solid composition with the highest melting point in binary Li-Sn system. Therefore,  $x = 82$  can be interpreted as the ideal Li-Sn coordination environment within the liquid alloy for minimizing D retention.

The diffusivity of Li (and Sn) atoms in the liquid alloy (Figure 6) displays non-monotonic trends with variations in  $\beta$ . These can be attributed to: i) an increase in the atom densities as  $\beta$  increases and ii) Li and D segregation towards  $\text{D}_2$  bubbles in the liquid. In addition, the diffusivity of Sn is less sensitive to changes in  $\beta$  compared to Li (Figure 6) primarily due to a lack of bonding between Sn and D. On the other hand, trends in the diffusivity of free D atoms and  $\text{D}_2$  molecules (Figure 6) are governed by: i) the clustering of  $\text{D}_2$  molecules that creates a concentration gradient (at low  $\beta$ ) and ii) the formation of  $\text{D}_2$  bubbles (at high  $\beta$ ) that facilitates diffusion of free D atoms around the surface of the bubble. Interestingly, the self-diffusion of the  $\text{D}_2$  gas bubble (Figure 7) is lower than any Li, Sn, free D, or free  $\text{D}_2$  species located within the liquid alloy.

Lastly, we computed the viscosity of liquid  $\text{Li}_{130}\text{Sn}_{70}\text{D}_\beta$  (Figure 8) and compared it to the viscosity of pure liquid  $\text{Li}_{130}\text{Sn}_{70}$  and liquid  $\text{LiD}_\beta$  [21,25]. Notably, the viscosity of liquid  $\text{Li}_{130}\text{Sn}_{70}\text{D}_\beta$  is significantly higher than pure  $\text{Li}_{130}\text{Sn}_{70}$ , i.e., the viscosity increases dramatically once D atoms are added to the liquid

alloy. A similar effect is observed for the case of D addition to pure liquid Li, which points to the interactions between Li and D atoms as the primary cause for this increase in viscosity, possibly including the formation of solid LiD nuclei in the liquid.

Overall, liquid  $\text{Li}_{30}\text{Sn}_{70}$  seems to be a promising candidate as a PFC due to the following conclusions from our study, which also corroborate with available experimental data. First, liquid  $\text{Li}_{30}\text{Sn}_{70}$  has a low D solubility (Figures 3 and 5) thereby avoiding fuel retention. Second, the fast diffusion of D and  $\text{D}_2$  (Figure 6) will prevent the formation of  $\text{D}_2$  bubbles in the liquid if the rate of D bombardment is low, i.e., the equilibrium D concentration in the liquid remains lower than  $\beta = 22.5$ . Once the free D atoms diffuse towards the surface of the liquid film, their tendency to form  $\text{D}_2$  molecules will increase, facilitating their escape into the gas/vacuum adjacent to the liquid. Thus, at low rates of D bombardment,  $\text{D}_2$  bubble formation and detrimental fuel retention will not be a concern for liquid  $\text{Li}_{30}\text{Sn}_{70}$ . However, for higher rates of D bombardment, the fast diffusion of D and  $\text{D}_2$  will facilitate the formation of  $\text{D}_2$  bubbles, which could increase sputtering of the liquid. The sluggish diffusion of  $\text{D}_2$  bubbles (Figure 7) within the liquid also will detrimentally increase the amount of fuel retained within the PFC. Finally, the increase in the viscosity of liquid  $\text{Li}_{30}\text{Sn}_{70}\text{D}_\beta$  versus pure  $\text{Li}_{30}\text{Sn}_{70}$  (Figure 8), mainly attributed to the interaction between Li and free D atoms, is largely limited by the formation of  $\text{D}_2$  molecules and the insignificant increase in the total amount of free D retained with increasing  $\beta$ . Indeed, the relative viscosity increase in liquid  $\text{Li}_{30}\text{Sn}_{70}\text{D}_\beta$  (versus  $\text{Li}_{30}\text{Sn}_{70}$ ) is lower than the relative increase observed in  $\text{LiD}_\beta$  versus liquid Li. Therefore, PFC mechanisms adopted for liquid Li should also be applicable for liquid  $\text{Li}_{30}\text{Sn}_{70}$ .

An immediate extension of our work is the study of the static and dynamic properties of  $\text{Li}_{30}\text{Sn}_{70}$  in the liquid film configuration, i.e., including the vacuum region, which will be a more realistic description of a practical PFC but will entail a significantly higher computational expense. Simulating the liquid film configuration also will enable capturing interactions with incident D atoms and the influence of different D bombardment rates. Li segregation to the liquid surface, along with variations of liquid properties at different depths of the film, will have an important effect on the interaction of the liquid with D and therefore requires further investigation.

## Acknowledgements

This work was supported in part by the Office of Naval Research (Grant No. 25700-G0001-10007802-101), Princeton University School of Engineering and Applied Science, and the Princeton Plasma Physics Laboratory (which is funded by the U.S. Department of Energy). The authors thank the Computational Science and Engineering Support (CSES) group at Princeton University for maintaining the Terascale

Infrastructure for Groundbreaking Research in Science and Engineering (TIGRESS). The authors are indebted to Ms. Nari Baughman for careful editing of this manuscript.

## Bibliography

- [1] Chou C B, Jhaveri J, Baldwin J W, Hannam P M, Keller K, Peng W, Rabin S, Ravikumar A P, Trierweiler A M, Wang X T and Socolow R 2016 Fusion Energy via Magnetic Confinement. An Energy Technology Distillate from the Andlinger Center for Energy and the Environment at Princeton University. 1–34 (<https://acee.princeton.edu/distillates/fusion-energy-via-magnetic-confinement/#introduction>)
- [2] Pitts R A, Carpentier S, Escourbiac F, Hirai T, Komarov V, Lisgo S, Kukushkin A S, Loarte A, Merola M, Sashala Naik A, Mitteau R, Sugihara M, Bazylev B and Stangeby P C 2013 A full tungsten divertor for ITER: Physics issues and design status *J. Nucl. Mater.* **438** S48–56
- [3] Coenen J W, De Temmerman G, Federici G, Philipps V, Sergienko G, Strohmayer G, Terra A, Unterberg B, Wegener T and Van den Bekerom D C M 2014 Liquid metals as alternative solution for the power exhaust of future fusion devices: status and perspective *Phys. Scr.* **T159** 014037
- [4] Nygren R E, Harjes H C, Wakeland P, Ellis R, Kugel H W, Kaita R, Berzak L, Zakharov L and Ehrhart B 2009 Thermal control of the liquid lithium divertor for NSTX **84** 1438–41
- [5] Mirnov S 2009 Plasma-wall interactions and plasma behaviour in fusion devices with liquid lithium plasma facing components *J. Nucl. Mater.* **390–391** 876–85
- [6] Nygren R E and Tabarés F L 2016 Liquid surfaces for fusion plasma facing components—A critical review. Part I: Physics and PSI *Nucl. Mater. Energy* **9** 6–21
- [7] Stangeby P 2000 *The Plasma Boundary of Magnetic Fusion Devices* (Bristol: Institute of Physics Publishing)
- [8] Pütterich T, Neu R, Dux R, Whiteford A D, O’Mullane M ., Summers H P and Team A U 2010 Calculation and experimental test of the cooling factor of tungsten *Nucl. Fusion* **50** 025012
- [9] Mansfield D K, Johnson D W, Grek B, Kugel H W, Bell M G, Bell R E, Budny R V, Bush C E, Fredrickson E D, Hill K W, Jassby D L, Maqueda R J, Park H K, Ramsey A T, Synakowski E J, Taylor G and Wurden G A 2001 Observations concerning the injection of a lithium aerosol into the edge of TFTR discharges Observations concerning the injection of a lithium aerosol *Nucl. Fusion* **41** 1823

- [10] Majeski R, Kaita R, Boaz M, Efthimion P, Gray T, Jones B, Hoffman D, Kugel H, Menard J, Munsat T, Post-zwicker A, Spaleta J, Taylor G, Timberlake J, Woolley R, Zakharov L, Finkenthal M, Stutman D, Antar G, Doerner R, Luckhardt S, Seraydarian R, Maingi R, Maiorano M, Smith S, Rodgers D and Soukhanovskii V 2004 Testing of liquid lithium limiters in CDX-U *Fusion Eng. Des.* **72** 121–32
- [11] Morgan T W, Rindt P, Eden G G Van, Kvon V, Jaworksi M A and Cardozo N J L 2018 Liquid metals as a divertor plasma-facing material explored using the Pilot-PSI and Magnum-PSI linear devices *Phys. Control. Fusion* **60** 014025
- [12] Loureiro J P S, Fernandes H, Tabarés F L, Mazzitelli G, Silva C, Gomes R, Alves E, Mateus R, Pereira T, Figueiredo H and Alves H 2017 Deuterium retention in tin ( Sn ) and lithium – tin ( Li – Sn ) samples exposed to ISTTOK plasmas *Nucl. Mater. Energy* **12** 709–13
- [13] Übeyli M 2003 On the tritium breeding capability of Flibe, Flinabe, and Li 20Sn80 in a fusion-fission (hybrid) reactor *J. Fusion Energy* **22** 51–7
- [14] Moriyama H, Sagara A, Tanaka S, Moir R W and Sze D K 1998 Molten salts in fusion nuclear technology *Fusion Eng. Des.* **40** 627–37
- [15] Smith D L, Baker C C, Sze D K, Morgan G D, Abdou M A, Plet S J, Schultz K R, Moir R W and Gordon J D 1985 Overview of the Blanket Comparison and Selection Study *Fusion Technol.* **8** 1P1
- [16] Abdou M A, Team T A, Ying A, Morley N, Gulec K, Smolentsev S, Kotschenreuther M, Malang S, Zinkle S, Rognlien T, Fogarty P, Nelson B, Nygren R, McCarthy K, Youssef M Z, Ghoniem N, Sze D, Wong C, Sawan M, Khater H, Woolley R, Mattas R, Moir R, Sharafat S, Brooks J, Hassanein A, Petti D, Tillack M, Ulrickson M and Uchimoto T 2001 On the exploration of innovative concepts for fusion chamber technology *Fusion Eng. Des.* **54** 181–247
- [17] Mattas R F, Allain J P, Bastasz R, Brooks J N, Evans T, Hassanein A, Luckhardt S, McCarthy K, Mioduszewski P, Maingi R, Mogahed E, Moir R, Molokov S, Morely N, Nygren R, Rognlien T, Reed C, Ruzic D, Sviatoslavsky I, Sze D, Tillack M, Ulrickson M, Wade P M, Wooley R and Wong C 1999 *ALPS-Advanced Limiter-divertor Plasma-facing Systems*
- [18] Rognlien T D and Rensink M E 2001 Interactions between liquid-wall vapor and edge plasmas *J. Nucl. Mater.* **293** 312–6
- [19] Bastasz R and Eckstein W 2001 Plasma - surface interactions on liquids *J. Nucl. Mater.* **290–293**



- [20] Suchonová M, Kristof J, Pribula M, Veis M, Tabarés F L and Veis P 2017 Analysis of LiSn alloy at several depths using LIBS *Fusion Eng. Des.* **117** 175–9
- [21] del Rio B G, de Jong E K and Carter E A 2019 Properties of fusion-relevant liquid Li-Sn alloys: An ab initio molecular-dynamics study *Nucl. Mater. Energy* **18** 326–30
- [22] Tabarés F L, Oyarzabal E, Martin-Rojo A B, Tafalla D, de Castro A, Medina F, Ochando M A, Zurro B and McCarthy K 2017 Experimental tests of LiSn alloys as potential liquid metal for the divertor target in a fusion reactor *Nucl. Mater. Energy* **12** 1368–73
- [23] Kang Y and Terai T 2004 In-reactor experiment and the tritium diffusion coefficient in molten lithium-tin alloy *J. Nucl. Mater.* **329–333** 1318–21
- [24] Kang Y and Terai T 2005 Tritium transport behavior in the molten lithium-tin alloy *J. Phys. Chem. Solids* **66** 615–8
- [25] Chen M, Abrams T, Jaworski M A and Carter E A 2016 Rock-salt structure lithium deuteride formation in liquid lithium with high-concentrations of deuterium: a first-principles molecular dynamics study *Nucl. Fusion* **56** 016020
- [26] Abrams T, Jaworski M A, Kaita R, Nichols J H, Stotler D P, Temmerman G De, Berg M A Van Den, Meiden H J Van Der and Morgan T W 2015 Modeling the reduction of gross lithium erosion observed under high-flux deuterium bombardment *J. Nucl. Mater.* **463** 1169–72
- [27] Abrams T, Jaworski M A, Chen M, Carter E A, Kaita R, Stotler D P, Temmerman G De, Morgan T W, Berg M A Van Den and Meiden H J Van Der 2016 Suppressed gross erosion of high-temperature lithium via rapid deuterium implantation *Nucl. Fusion* **56** 016022
- [28] Kohn W and Sham L J 1965 Self-consistent equations including exchange and correlation effects *Phys. Rev.* **140** A1133–8
- [29] Kresse G and Furthmüller J 1996 Efficient iterative schemes for ab initio total-energy calculations using a plane-wave basis set *Phys. Rev. B* **54** 11169–86
- [30] Kresse G and Furthmüller J 1996 Efficiency of ab-initio total energy calculations for metals and semiconductors using a plane-wave basis set *J. Comput. Mater. Sci.* **6** 15–50
- [31] Blöchl P E 1994 Projector augmented-wave method *Phys. Rev. B* **50** 17953–79
- [32] Kresse G 1999 From ultrasoft pseudopotentials to the projector augmented-wave method *Phys.*

*Rev. B* **59** 1758–75

- [33] Perdew J P, Burke K and Ernzerhof M 1996 Generalized Gradient Approximation Made Simple *Phys. Rev. Lett.* **77** 3865–8
- [34] Perdew J P, Ruzsinszky A, Csonka G I, Vydrov O A, Scuseria G E, Constantin L A, Zhou X and Burke K 2008 Restoring the Density-Gradient Expansion for Exchange in Solids and Surfaces *Phys. Rev. Lett.* **100** 136406
- [35] Ceperley D M and Alder B J 1980 Ground state of the electron gas by a stochastic method *Phys. Rev. Lett.* **45** 566–9
- [36] Perdew J P and Zunger A 1981 Self-interaction correction to density-functional approximations for many-electron systems *Phys. Rev. B* **23** 5048–79
- [37] Monkhorst H J and Pack J D 1976 Special points for Brillouin-zone integrations. *Phys. Rev. B* **13** 5188–92
- [38] Methfessel M and Paxton A T 1989 High-precision sampling for Brillouin-zone integration in metals *Phys. Rev. B* **40** 3616–21
- [39] Belsky A, Hellenbrandt M, Karen V L and Luksch P 2002 New developments in the Inorganic Crystal Structure Database (ICSD): accessibility in support of materials research and design *Acta Cryst.* **B58** 364–9
- [40] Yin F, Su X, Li Z and Wang J 2005 Thermodynamic assessment of the Li-Sn (Lithium-Tin) system *J. Alloys Compd.* **393** 105–8
- [41] Songster J and Pelton A D 1993 The H-Li (Hydrogen-Lithium) System *J. Phase Equilib.* **14** 373–81
- [42] Nosé S 1984 A unified formulation of the constant temperature molecular dynamics methods *J. Chem. Phys.* **81** 511–9
- [43] Hoover W G 1985 Canonical dynamics: Equilibrium phase-space distributions *Phys. Rev. A* **31** 1695–7
- [44] Balucani U and Zoppi M 1994 *Dynamics of the liquid state* (Oxford: Clarendon Press)
- [45] van Hove L 1954 Correlations in Space and Time and Born Approximation Scattering in Systems of Interacting Particles *Phys. Rev.* **95** 249–62

- [46] Bryk T and Mryglod I 2000 Generalized hydrodynamics of binary liquids: Transverse collective modes *Phys. Rev. E* **62** 2188–99
- [47] Zwanzig R 1961 Memory effects in irreversible thermodynamics *Phys. Rev.* **124** 983
- [48] Mori H 1965 Transport, Collective Motion, and Brownian Motion *Prog. Theor. Phys.* **33** 423–55
- [49] Balucani U, Brodholt J P, Jedlovsky P and Vallauri R 2000 Viscosity of liquid water from computer simulations with a polarizable potential model *Phys. Rev. E* **62** 2971–3
- [50] Messer C E and Levy I S 1965 Systems of Lithium Hydride with Alkaline Earth and Rare Earth Hydrides *Inorg. Chem.* **4** 543–8
- [51] Baldwin M J, Doerner R P, Causey R, Luckhardt S C and Conn R W 2002 Recombination of deuterium atoms on the surface of molten Li – LiD *J. Nucl. Mater.* **306** 15–20
- [52] Baldwin M J, Doerner R P, Luckhardt S C, Seraydarian R, Whyte D G and Conn R W 2002 Plasma interaction with liquid lithium : Measurements of retention and erosion **62** 231–6
- [53] Krasin V P and Soyustova S I 2018 Quantitative evaluation of thermodynamic parameters of Li-Sn alloys related to their use in fusion reactor *J. Nucl. Mater.* **505** 193–9
- [54] Schumacher R and Weiss A 1990 Hydrogen Solubility in the Liquid Alloys Lithium-Indium, Lithium-Lead, and Lithium-Tin *Ber. Bunsenges. Phys. Chem.* **94** 684–91
- [55] Ong S P, Richards W D, Anubhav J, Hautier G, Kocher M, Cholia S, Gunter D, Chevrier V L, Persson K A and Ceder G 2013 Python Materials Genomics (pymatgen): A robust, open-source python library for materials analysis *Comput. Mater. Sci.* **68** 314–9
- [56] Linstrom P J and Mallard W G 2019 *NIST Chemistry WebBook, NIST Standard Reference Database Number 69* (Gaithersburg, MD, 20899: National Institute of Standards and Technology)
- [57] Wang M, Sun W, Sha C, Hu B, Du Y, Sun L, Xu H, Wang J and Liu S 2012 Thermodynamic Modeling of the Li-H and Ca-H Systems *J. Phase Equilib. Diff.* **33** 89–96
- [58] Muggianu Y-M, Gambino M and Bros J-P 1975 Enthalpies de formation des alliages liquides bismuth-étain-gallium à 723 k. Choix d’une représentation analytique des grandeurs d’excès intégrales et partielles de mélange *J. Chim. Phys.* **72** 83–8
- [59] Bruson A and Gerl M 1980 Diffusion Coefficient of 113 Sn, 124 Sb, 110m Ag, and 195 Au in Liquid Sn *Phys. Rev. B* **21** 5447–54

- [60] Shpil'rain E E, Yakimovich K A, Fomin V A, Skovorodjko S N and Mozgovoï A G 1985 *Handbook of Thermodynamic and Transport Properties of Alkali Metals* ed R W Ohse (Blackwell, Oxford)
- [61] Plevachuk Y, Sklyarchuk V, Hoyer W and Kaban I 2006 Electrical conductivity, thermoelectric power and viscosity of liquid Sn-based alloys *J. Mater. Sci.* **41** 4632–5